

Two-dimensional polyaniline crystal with metallic out-of-plane conductivity

<https://doi.org/10.1038/s41586-024-08387-9>

Received: 20 February 2022

Accepted: 11 November 2024

Published online: 5 February 2025

 Check for updates

Tao Zhang^{1,2,21}, Shu Chen^{3,19,21}, Petko St. Petkov^{4,21}, Peng Zhang^{1,21}, Haoyuan Qi^{1,5,21}, Nguyen Ngan Nguyen^{1,6,21}, Wenjie Zhang⁶, Jiho Yoon⁶, Peining Li^{3,7}, Thomas Brumme⁸, Alexey Alfonsov⁹, Zhongquan Liao¹⁰, Mike Hambach¹¹, Shunqi Xu¹, Lars Mester^{3,20}, Vladislav Kataev⁹, Bernd Büchner^{9,12}, Stefan C. B. Mannsfeld¹¹, Ehrenfried Zschech¹¹, Stuart S. P. Parkin⁶, Ute Kaiser⁵, Thomas Heine^{8,13,14}, Renhao Dong^{1,6}, Rainer Hillenbrand^{17,18} & Xinliang Feng^{1,6}

Linear conducting polymers show ballistic transport, imposed by mobile carriers moving along the polymer chains^{1,2}, whereas conductance in the extended dimension, that is, between polymer strands or layers, remains weak due to the lack of intermolecular ordering and electronic coupling^{3–5}. Here we report a multilayer-stacked two-dimensional polyaniline (2DPANI) crystal, which shows metallic out-of-plane charge transport with high electrical conductivity. The material comprises columnar π arrays with an interlayer distance of 3.59 Å and periodic rhombohedral lattices formed by interwoven polyaniline chains. Electron spin resonance spectroscopy reveals significant electron delocalization in the 2DPANI lattices. First-principles calculations indicate the in-plane 2D conjugation and strong interlayer electronic coupling in 2DPANI facilitated by the Cl-bridged layer stacking. To assess the local optical conductivity, we used terahertz and infrared nanospectroscopy to unravel a Drude-type conductivity with an infrared plasma frequency and an extrapolated local d.c. conductivity of around 200 S cm⁻¹. Conductive scanning probe microscopy showed an unusually high out-of-plane conductivity of roughly 15 S cm⁻¹. Transport measurements through vertical and lateral micro-devices revealed comparable high out-of-plane (roughly 7 S cm⁻¹) and in-plane conductivity (roughly 16 S cm⁻¹). The vertical micro-devices further showed increasing conductivity with decreasing temperature, demonstrating unique out-of-plane metallic transport behaviour. By using this multilayer-stacked 2D conducting polymer design, we predict the achievement of strong electronic coupling beyond in-plane interactions, potentially reaching three-dimensional metallic conductivity^{6,7}.

The charge transport properties and metallic states of linear conducting polymers have been extensively investigated since the reports on doped polyacetylene more than 40 years ago^{1–3,8}. So far, understanding of the charge carrier transport mechanisms in conducting polymers continues to receive increasing attention, especially regarding the rise of organic electronics^{4–11}. Because of the large intrachain coupling, charge transfer is thought to occur mainly along the conjugated chains,

but with interchain hopping as a crucial secondary contribution^{5,12}. To achieve an efficient charge transport in conducting polymers in extended dimensions, a direct approach is to enhance the intermolecular overlap of frontier orbitals to form dispersed bands^{3,13}.

In the past decades, tremendous efforts have been made to improve the linear chain alignment of conducting polymers, including polyacetylene^{1,14}, polythiophenes^{4,15,16} and polyaniline¹⁰, enabling the maximization

¹Faculty of Chemistry and Food Chemistry and Center for Advancing Electronics Dresden (caed), Technische Universität Dresden, Dresden, Germany. ²Key Laboratory of Advanced Marine Materials, Ningbo Institute of Materials Technology and Engineering, Chinese Academy of Sciences, Ningbo, China. ³CIC nanoGUNE BRTA, Donostia-San Sebastián, Spain. ⁴University of Sofia, Faculty of Chemistry and Pharmacy, Sofia, Bulgaria. ⁵Central Facility of Materials Science Electron Microscopy, Universität Ulm, Ulm, Germany. ⁶Max Planck Institute of Microstructure Physics, Halle (Saale), Germany. ⁷Wuhan National Laboratory for Optoelectronics and School of Optical and Electronic Information, Huazhong University of Science and Technology, Wuhan, China. ⁸Chair of Theoretical Chemistry, Technische Universität Dresden, Dresden, Germany. ⁹Leibniz Institute for Solid State and Materials Research Dresden, Dresden, Germany. ¹⁰Fraunhofer Institute for Ceramic Technologies and Systems (IKTS), Dresden, Germany. ¹¹Center for Advancing Electronics Dresden (caed) and Faculty of Electrical and Computer Engineering, Technische Universität Dresden, Dresden, Germany. ¹²Institute for Solid State and Materials Physics and Würzburg-Dresden Cluster of Excellence ct.qmat, Technische Universität Dresden, Dresden, Germany. ¹³Helmholtz-Zentrum Dresden-Rossendorf, Center for Advanced Systems Understanding (CASUS), Görlitz, Germany. ¹⁴Department of Chemistry and IBS Center for Nanomedicine, Yonsei University eodaemun-gu, Seoul, Republic of Korea. ¹⁵Department of Chemistry, The University of Hong Kong, Hong Kong, China. ¹⁶Materials Innovation Institute for Life Sciences and Energy (MILES), HKU-SIRI, Shenzhen, China. ¹⁷CIC nanoGUNE BRTA and EHU/UPV, Donostia-San Sebastián, Spain. ¹⁸IKERBASQUE, Basque Foundation for Science, Bilbao, Spain. ¹⁹Present address: Terahertz Technology Innovation Research Institute, National Basic Science Center-Terahertz Science and Technology Frontier, Terahertz Precision Biomedical Discipline 111 Project, Shanghai Key Laboratory of Modern Optical System, University of Shanghai for Science and Technology, Shanghai, China. ²⁰Present address: attocube systems AG, Haar, Germany. ²¹These authors contributed equally: Tao Zhang, Shu Chen, Petko St. Petkov, Peng Zhang, Haoyuan Qi, Nguyen Ngan Nguyen. [✉]e-mail: thomas.heine@tu-dresden.de; rhdong@hku.hk; r.hillenbrand@nanogune.eu; xinliang.feng@tu-dresden.de

of their interchain charge transport in two dimensions (in-plane)^{4,15} or even in three dimensions (in- and out-of-plane)^{5–7}. A very appealing strategy is to create ordered arrays of covalently linked conducting polymers^{17–19}. For instance, two-dimensional conducting polymers (2DCPs) are characterized by in-plane π -conjugated periodic molecular structures with conjugated crosslinks between chains, which provide intramolecular pathways for charge carriers^{20–23}. Despite the recent advancements in the synthesis of 2DCPs, the charge transport (that is, conductivity) within and between the 2D polymer layers remains limited or weak due to insufficient structural ordering and electronic coupling.

Here we report a multilayer-stacked 2D polyaniline (2DPANI) crystal with a domain size of 130–160 μm^2 and thickness from tens to hundreds of nanometres by means of a topology-directed 2D polymerization of aniline using surfactant monolayer-assisted on-water surface synthesis. We demonstrate that the 2DPANI comprises long-range ordered rhombohedral lattices ($a = b = 20.8 \text{ \AA}$, $\gamma = 115^\circ$) and AA-serrated stacked multilayers with an interlayer distance of $c = 3.59 \text{ \AA}$. Electron spin resonance (ESR) spectroscopy identifies a strong electron delocalization state in the 2DPANI at room temperature. First-principles calculations reveal the significant contributions from the extended 2D conjugation and compact layer stacking by van der Waals interaction as well as interlayer Cl[−] ion-bridging contribute to the strong interlayer-out-of-plane electronic coupling. Terahertz (THz) and infrared (IR) nanospectroscopy show a high optical conductivity, which can be explained by a three-dimensional (3D) Drude model with an IR plasma frequency and from which we extrapolate a d.c. conductivity of roughly 200 S cm^{−1}. Conductive atomic force microscopy (c-AFM) reveals high conductivity in the out-of-plane ($14.9 \pm 4.6 \text{ S cm}^{-1}$) direction. Electrical transport measurements using vertical micro-devices reveal a typical metallic charge transport behaviour (that is, monotonic decrease of resistance versus temperature from 300 to 3 K) in the out-of-plane direction of single 2DPANI flakes, with an average electrical conductivity of $7.1 \pm 3.4 \text{ S cm}^{-1}$ at room temperature.

Synthesis and structure

To achieve the synthesis of 2DPANI crystals, we used an anionic surfactant monolayer (sodium *n*-octadecyl sulfate) on a hydrochloric acid aqueous solution surface (0.75 M, namely surfactant monolayer-assisted interfacial synthesis) to control the pre-organization of the subsequently added aniline monomers (0.13 mmol) (Fig. 1a,b)^{24,25}. Ammonium persulfate (0.02 mmol) was then added into the subphase to initiate the polymerization. The reaction was kept at 1 °C under ambient conditions for roughly 72 h to produce 2DPANI flakes on the water surface (Fig. 1c,d and Supplementary Fig. 1). The flakes were fished using arbitrary substrates and appeared as oval-shaped crystals when observed by light microscopy (Fig. 2a and Supplementary Fig. 2). In a count of roughly 85 flakes, the average domain size (in terms of length) was estimated as $15.6 \pm 2.3 \mu\text{m}$ (that is, domain area 130–160 μm^2 ; Supplementary Figs. 3 and 4). Using AFM, the average thickness of a selected flake was determined to be roughly 92 nm (Supplementary Fig. 5). We note that both on-water surface and surfactant monolayer are key factors for determining the formation of 2DPANI: (1) they facilitate the simultaneous pre-organization and polymerization of aniline monomers into ordered polymer chains under the anionic head groups of surfactant monolayer; and (2) they also provide a confined environment (between surfactant monolayer and water surface) for the formation of 2DPANI lattices. The result demonstrates that 2DPANI can be synthesized from individual monomers (for example, aniline), in contrast to the current general conception that two or more monomers are needed for the construction of organic 2D polymers²⁶. The resultant 2DPANI was intrinsically doped by hydrochloric acid during the surfactant monolayer-assisted interfacial synthesis.

We investigated the composition of individual 2DPANI flakes through micro-X-ray photoelectron spectroscopy (μ -XPS) (Supplementary Fig. 6

and Table 1), which revealed C, N and Cl elements. Deconvolution of the C1s signal generates three peaks, assignable to the C1s of C–C at 284.8 eV, C–N at 286.5 eV and π – π^* shake-up from the phenyl rings at 288.2 eV (Supplementary Fig. 7a), respectively. Two prominent peaks of N1s at 401.9 and 399.8 eV correspond to the two types of nitrogen (−NH⁺ and −NH−) in 2DPANI (Supplementary Fig. 7b,e), which are consistent with the calculated XPS spectra (Supplementary Fig. 7c,d).

We next investigated the crystal structure of 2DPANI using grazing-incidence wide-angle X-ray scattering (GIWAXS) (Fig. 2b and Supplementary Fig. 8). The strong in-plane scattering peaks near $Q_z = 0$ show that most 2DPANI crystals are aligned parallel to the substrate surface with lattice parameters of $a = b = 20.9 \text{ \AA}$ and $\gamma = 114.8^\circ$. The broad lamellar stacking arc at a Q_z of 1.75 \AA^{-1} corresponds to an average out-of-plane stacking distance d_{001} of roughly 3.59 \AA (Fig. 2b). Please note that whereas d_{001} can be determined from the GIWAXS data, accurate values for α and β cannot be given, owing to a possible long-range rotational disorder that produces the broad out-of-plane signal (details can be found in the GIWAXS methods). Selected area electron diffraction (SAED) on 2DPANI shows typical single-crystalline diffraction patterns of a rhombic lattice with the nearest reflections corresponding to $a = b = 20.9 \text{ \AA}$, $\gamma = 115^\circ$ (Fig. 2c and Supplementary Figs. 9–11)²⁴, which match well with the GIWAXS results. Based on the experimental values, a periodic structural model with the serrated-AA stacking was constructed and fully optimized using density-functional theory (DFT). The optimized structural parameters agree with the GIWAXS and SAED experiments, yielding lattice parameters of $a = b = 20.8 \text{ \AA}$, $c = 3.52 \text{ \AA}$, $\alpha = \beta = 90.0^\circ$, $\gamma = 115^\circ$. In an energy-minimized structure, we identify that the Cl[−] ions are located in the pores and bridge the neighbouring 2DPANI layers, with −NH–Cl[−]–HN– connection in a roughly 2.1 \AA distance (Fig. 2f–h, Supplementary Figs. 12–15 and Table 2), which enhances the interaction between the layers.

We then carried out the aberration-corrected high-resolution transmission electron microscopy (AC-HRTEM) imaging for the direct observation of 2DPANI crystals²⁷. An image resolution of 2.2 \AA has been achieved and domain edges can be clearly visualized (Fig. 2d and Supplementary Fig. 16). Under the experimental imaging conditions, the 2DPANI appears bright on a dark background (Fig. 2e). The close resemblance between experimental and simulated SAED patterns as well as AC-HRTEM images validates the serrated-AA stacking model (Fig. 2e insets and Supplementary Fig. 17). We note that cracks and defects have been observed occasionally (Supplementary Fig. 18), which could be attributed to growth errors, mechanical stress during film transfer and/or electron irradiation damage.

ESR and DFT study

We further probed the unpaired electrons in 2DPANI by ESR spectroscopy (Supplementary Figs. 19 and 20). In the temperature range of 5–300 K, the ESR spectrum shows a single line, which can be well fitted with a Lorentzian line profile (Fig. 3a). From such a fit, we determine the integrated intensity of the signal I_{ESR} , its width ΔH and the field of resonance H_{res} , yielding a g factor of $g = h\nu/(\mu_B H_{\text{res}}) \approx 2.002$ (Supplementary Fig. 20a). Given the closeness of the g factor to the free electron value and a relatively narrow Lorentzian-shaped ESR line profile, the observed ESR signal can be attributed to the response of unpaired electrons. In the range of 5–100 K, the intensity I_{ESR} , which is proportional to the static spin susceptibility of the unpaired electrons χ_{spin} , decreases with increasing T (Fig. 3b), suggesting that χ_{spin} in this regime follows the Curie law temperature dependence $\chi_{\text{spin}} \propto 1/T$. Above a characteristic temperature $T^* \approx 100 \text{ K}$, the ESR intensity and thus the spin susceptibility stay practically constant within the error bars. The value $T^* \approx 100 \text{ K}$ can also be determined from the T dependence of the g factor (Supplementary Fig. 20a) and the linewidth (Supplementary Fig. 20b). Similar behaviour of the spin susceptibility was also observed in the other 2DPANI samples (Supplementary Figs. 21 and 22), indicating a high reproducibility.

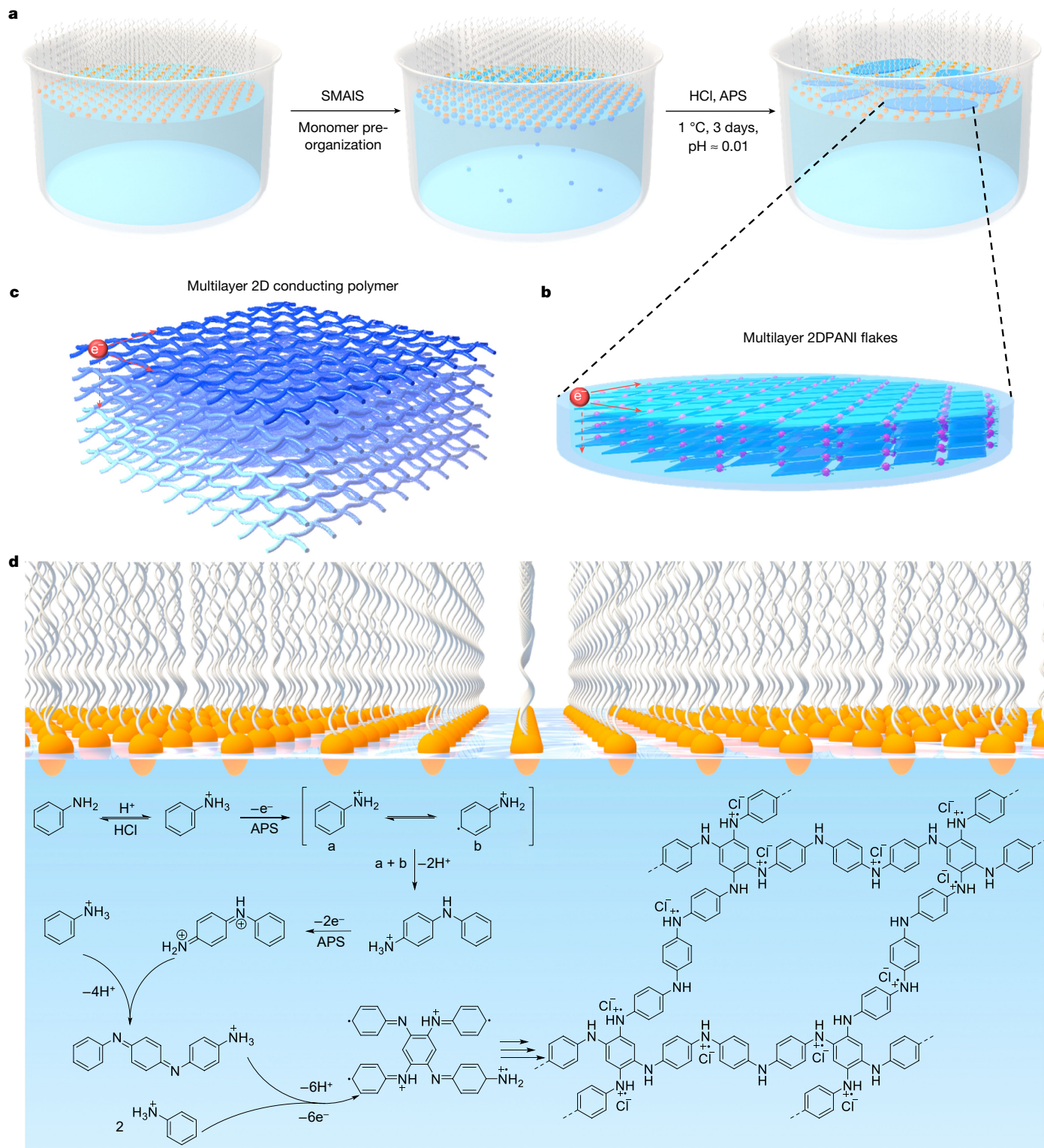


Fig. 1 | Schematic illustration of the synthesis procedure and proposed molecular structure for 2DPANI. **a,b**, Schematic of the on-water surface synthesis procedure for 2DPANI (**a**) and the multilayer 2DPANI flakes formed on the water surface (**b**). **c**, Schematic of charge transport in multilayer-stacked 2D conducting polymer, in which the red balls are the electrons and the surrounding

solid and dashed arrows indicate intrachain and/or -layer transport and interchain and/or -layer transport of each electron, respectively. **d**, A proposed mechanism for the polymerization on the water surface (for simplicity, the Cl^- counter ions are not shown) and molecular structure of 2DPANI. APS, ammonium persulfate; SMAIS, surfactant monolayer-assisted interfacial synthesis.

The Curie law type T -dependence of their spin susceptibility at $T < T^*$ evidences the localized character of the unpaired electrons, which can be considered free radical centres. Comparing I_{ESR} in this regime with that of the standard reference sample (that is, Al_2O_3 doped by Cr^{3+}), we estimate the spin density, which amounts to roughly 0.22 spins per

unit cell, which is lower than the number of charged nitrogen (roughly four) per unit cell, probably due to the existence of bipolaron lattices²⁸. By contrast, the nearly constant value of $I_{\text{ESR}} \propto \chi_{\text{spin}}$ at $T > T^*$ suggests a Pauli-like spin susceptibility of the resonating spins (Fig. 3b), which is a fingerprint of the delocalized electrons. The delocalized character of

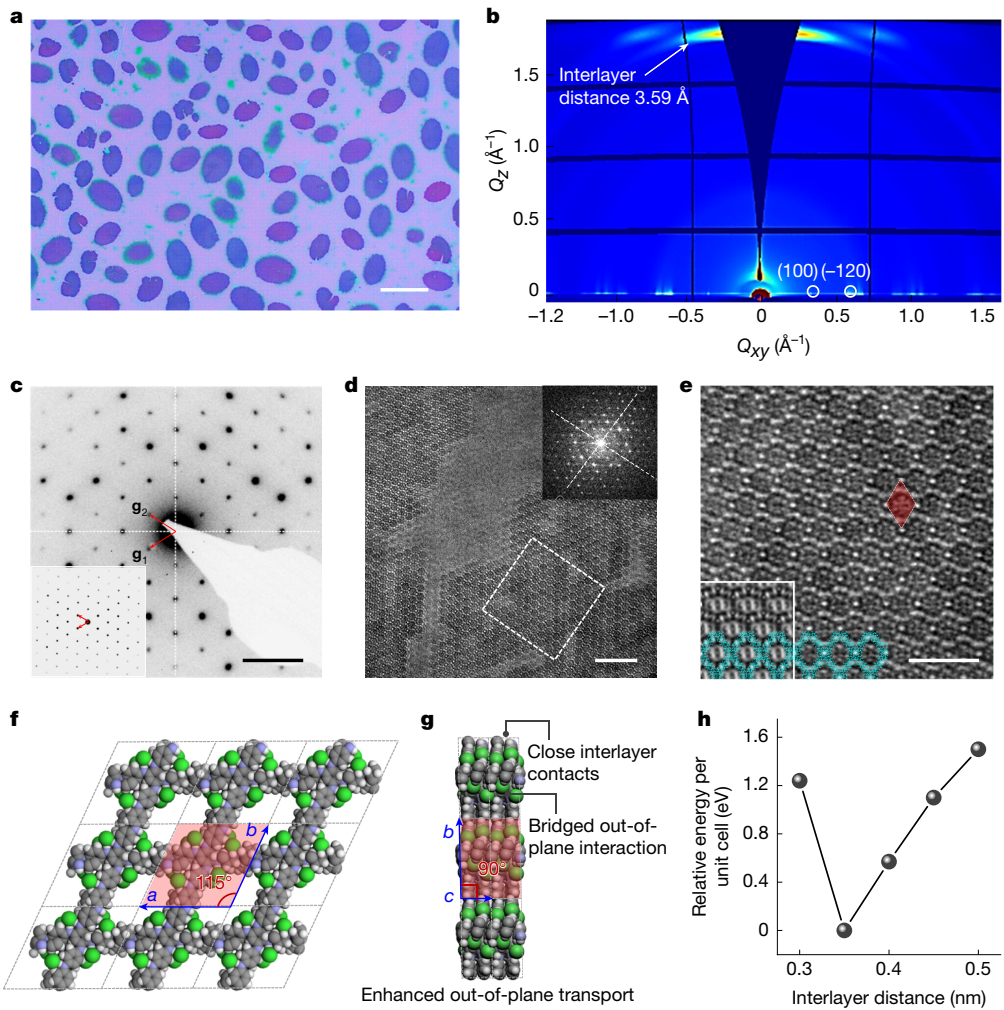


Fig. 2 | Morphology and structural characterizations of 2DPANI crystals. **a–c**, Light microscopy image of 2DPANI on SiO_2/Si (**a**), 2D GIWAXS plot of 2DPANI on Si wafer (**b**) and SAED pattern of 2DPANI (**c**). The angle between the reciprocal lattice vectors \mathbf{g}_1 and \mathbf{g}_2 is 65° and $|\mathbf{g}_1| = |\mathbf{g}_2| = 0.53 \text{ nm}^{-1}$. The white dashed lines mark the mirror planes. Inset, simulated image (thickness 84 nm, defocus 300 nm) with the DFT model overlaid, and the red rhombus indicates a unit cell. **d,g**, Reconstructed crystal structure at top (**f**) and side (**g**) views. The 2D layers are stacked at 3.52 Å intervals and connected by Cl^- along the z direction. **h**, Calculated relative energy per unit cell versus layers distance in multilayer 2DPANI. Scale bars, 20 μm (**a**), 1 nm^{-1} (**c**), 10 nm (**d**) and 5 nm (**e**).

(as marked by white box). The 2DPANI network appears bright on a dark background. Inset, simulated image (thickness 84 nm, defocus 300 nm) with the DFT model overlaid, and the red rhombus indicates a unit cell. **f,g**, Reconstructed crystal structure at top (**f**) and side (**g**) views. The 2D layers are stacked at 3.52 Å intervals and connected by Cl^- along the z direction. **h**, Calculated relative energy per unit cell versus layers distance in multilayer 2DPANI. Scale bars, 20 μm (**a**), 1 nm^{-1} (**c**), 10 nm (**d**) and 5 nm (**e**).

the electrons is also corroborated by the increased linewidth at higher temperatures due to an enhanced spin-lattice relaxation caused by the momentum scattering of the mobile particles (Supplementary Fig. 20b). Thus, the temperature $T^* \approx 100 \text{ K}$ can be identified as a characteristic crossover temperature for the electron delocalization in the 2DPANI²⁹. The DFT calculated iso-surface of the spin density and electron densities for the 2DPANI model demonstrate that π electrons are delocalized over the 2DPANI lattice (Fig. 3c and Supplementary Fig. 23), which agrees with the ESR results. By contrast, we note that the ESR intensity and thus the concentration of the unpaired electrons is markedly suppressed in the dedoped 2DPANI (for example, by treatment with 1 M NH_4OH , Supplementary Fig. 24).

To explain the origin of the interlayer electronic coupling, the electronic band structure and the projected density of states (PDOS) for both monolayer and multilayer 2DPANI models are calculated (Fig. 3d,e). Whereas the 2DPANI monolayer is a semimetal, the multilayer structure becomes metallic, in which the Cl^- ions and the interlayer $\pi-\pi$ interaction cause a substantial difference in the band structures of monolayer (Fig. 3d) and layer-stacked 2DPANI (Fig. 3e). On the basis of the monolayer model, the DFT calculations suggest no preference

for HCl doping of the different C–N–C groups (Supplementary Fig. 25) with preferable location of the Cl^- ions in the pore. Different initial alignments of the Cl^- ions around the –NH groups are considered, but the geometry optimizations always converge to the minimum where the Cl^- ions are allocated in the pore. Analysis of the PDOS shows that in the monolayer, where the interlayer interaction is missing, mainly the C(p) and N(p) levels contribute to the bands close to the Fermi level, whereas the Cl(p) levels are about $\pm 0.5 \text{ eV}$ away from the Fermi level. On stacking, because of the $\pi-\pi$ interaction and the bridging role of the Cl^- ions and closer interlayer contacts (roughly 3.4 Å), the Cl(p) levels shift closer to the Fermi level, thus mixing stronger with C and N p-levels to form a band with strong dispersion (0.40 eV) in the out-of-plane direction (Fig. 3e and Supplementary Fig. 26).

Frequency-dependent conductivity

The optical conductivity of individual 2DPANI flakes was probed using THz and IR scattering-type scanning near-field microscopy (s-SNOM) and Fourier transform IR nanospectroscopy (nano-FTIR)^{30,31}. To that end, 2DPANI flakes were transferred onto a 50 nm-thick Au layer on Si.

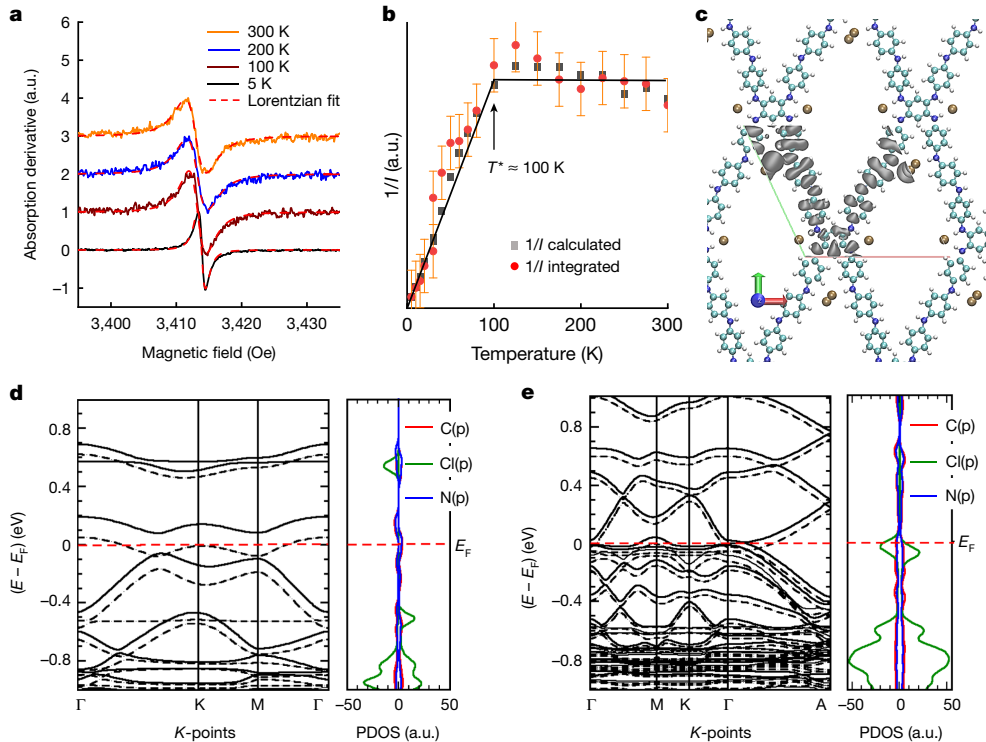


Fig. 3 | Electronic properties of 2DPANI by ESR studies and DFT calculations.

a, ESR spectra, measured at different temperatures (solid lines), together with their Lorentzian fits (dashed lines). **b**, Integrated (solid circles) and calculated from the fit (solid squares) inverse ESR intensity $1/I_{\text{ESR}} \propto \chi_{\text{spin}}^{-1}$ as a function of temperature in a range of 5–300 K. Note a crossover from the Curie law T -dependence at $T < T^* \approx 100$ K to a Pauli-like temperature-independent

behaviour at $T > T^*$. **c**, Visualization of the iso-surface of the spin density in the monolayer of 2DPANI structure, with two unpaired spins per unit cell ($\rho = 0.005$ electrons per \AA^3). Colour code: blue, N; ochre, Cl; cyan, C and white, H. **d,e**, Electronic band structures (left panel) and PDOS (right panel) of monolayer (**d**) and layer-stacked (**e**) 2DPANI. Full and dashed lines refer to the spin-polarized bands carrying electrons of α and β spin, respectively.

As illustrated in Fig. 4a, THz or IR laser radiation was scattered at an AFM tip. Interferometric detection of the tip-scattered field yielded nanoscale-resolved THz/IR amplitude and phase images or spectra (Methods). In the amplitude images (Fig. 4b), the 2DPANI flakes appeared as bright as the Au substrate at $\nu = 84 \text{ cm}^{-1}$ (THz, middle panel) and slightly darker at 910 cm^{-1} (IR, bottom panel). By contrast, both IR and THz amplitude signals of dedoped 2DPANI flakes (with removed mobile carriers) reduced to about 30% of the Au substrate's signal (Fig. 4c), demonstrating that the large signal of 2DPANI was due to mobile carriers and high, spatially homogeneous optical conductivity.

The slightly reduced amplitude signal of 2DPANI at 910 cm^{-1} suggests a plasma frequency in the mid-IR range. To confirm this and quantify the mobile carrier response, we recorded amplitude- and phase-resolved s-SNOM images of pristine (Fig. 4f) and dedoped (Supplementary Fig. 27) 2DPANI at various THz and IR frequencies, measuring the contrast with the Au substrate (red and black symbols in Fig. 4d). We also recorded nano-FTIR amplitude and phase spectra (red and black lines in Fig. 4d, normalized to Au). Both methods show a large IR amplitude signal for pristine 2DPANI, decreasing with increasing wavenumber ν , along with a broad peak in the phase spectrum (red data). Dedoped crystals show significantly reduced amplitude and phase signals (black data), confirming that 2DPANI's spectral response is dominated by mobile carriers.

To determine the optical conductivity, $\sigma(\nu) = i\varepsilon_0 2\pi c v(1 - \varepsilon(\nu))$, where ε_0 is the vacuum permittivity, c the light velocity and $\varepsilon(\nu)$ the dielectric function, we fitted the s-SNOM and nano-FTIR data using the finite-dipole model of s-SNOM³². Assuming an isotropic 3D Drude model for the mobile carriers in 2DPANI, the fit (blue curves in Fig. 4d) yields a high-frequency permittivity of $\varepsilon_\infty = 5$, as well as screened plasma frequency and damping parameter (both expressed in wave-numbers) of $\nu_p = 3,300$ and $\gamma_p = 4,500 \text{ cm}^{-1}$, respectively, from which

the optical conductivity (Fig. 4e) and extrapolated d.c. conductivity of $\sigma_{\text{d.c.}} \approx 2.0 \times 10^2 \text{ S cm}^{-1}$ is obtained. In the future, extended spectroscopy studies and more sophisticated modelling may be needed for a more accurate determination of the free-carrier conductivity, as our analysis does not consider conduction anisotropy and optical conductivity contributions from molecular vibrations and interactions (we used a constant high-frequency permittivity as a fitting parameter for approximating all non-Drude contributions).

The assumption of a 3D conductivity and the experimentally determined plasma frequency are supported by conductivity calculations within the constant relaxation-time approximation of the Boltzmann transport equation³³ (Supplementary Figs. 28 and 29). For the in- and out-of-plane conductivity-to-scattering time ratios of layer-stacked 2DPANI, we found $(\sigma/\tau)_{\text{in}} = 1.02 \times 10^{19} \text{ S m s}^{-1}$ and $(\sigma/\tau)_{\text{out}} = 0.38 \times 10^{19} \text{ S m s}^{-1}$, respectively, which correspond to an anisotropic 3D conductivity rather than to a classical 2D conductivity. From the relation $(\sigma/\tau)_{\text{BoltzTrap2}} = (\sigma/\tau)_{\text{Drude}} = ne^2/m^*$ and the charge carrier density $n = 3.5 \times 10^{21} \text{ cm}^{-3}$ (obtained from the temperature-broadened density of states (DOS)), we determined the in- and out-of-plane effective electron masses $m_x^* = m_y^* = 10.17m_0$ and $m_z^* = 27.65m_0$, respectively. According to $\nu_p = \omega_p/(2\pi c)$, where $\omega_p = \sqrt{ne^2/(\varepsilon_\infty \varepsilon_0 m^*)}$ is the screened plasma frequency, m^* the average effective mass and $\varepsilon_\infty = 5$, we obtain $\nu_p \approx 2,200 \text{ cm}^{-1}$, supporting the result obtained from IR nanospectroscopy.

Electrical transport

We first performed out-of-plane electrical transport measurements using micro-devices that were fabricated with single 2DPANI flakes (Supplementary Figs. 30 and 31). The measurements show a monotonic increase of the flake's conductivity when the temperature decreases

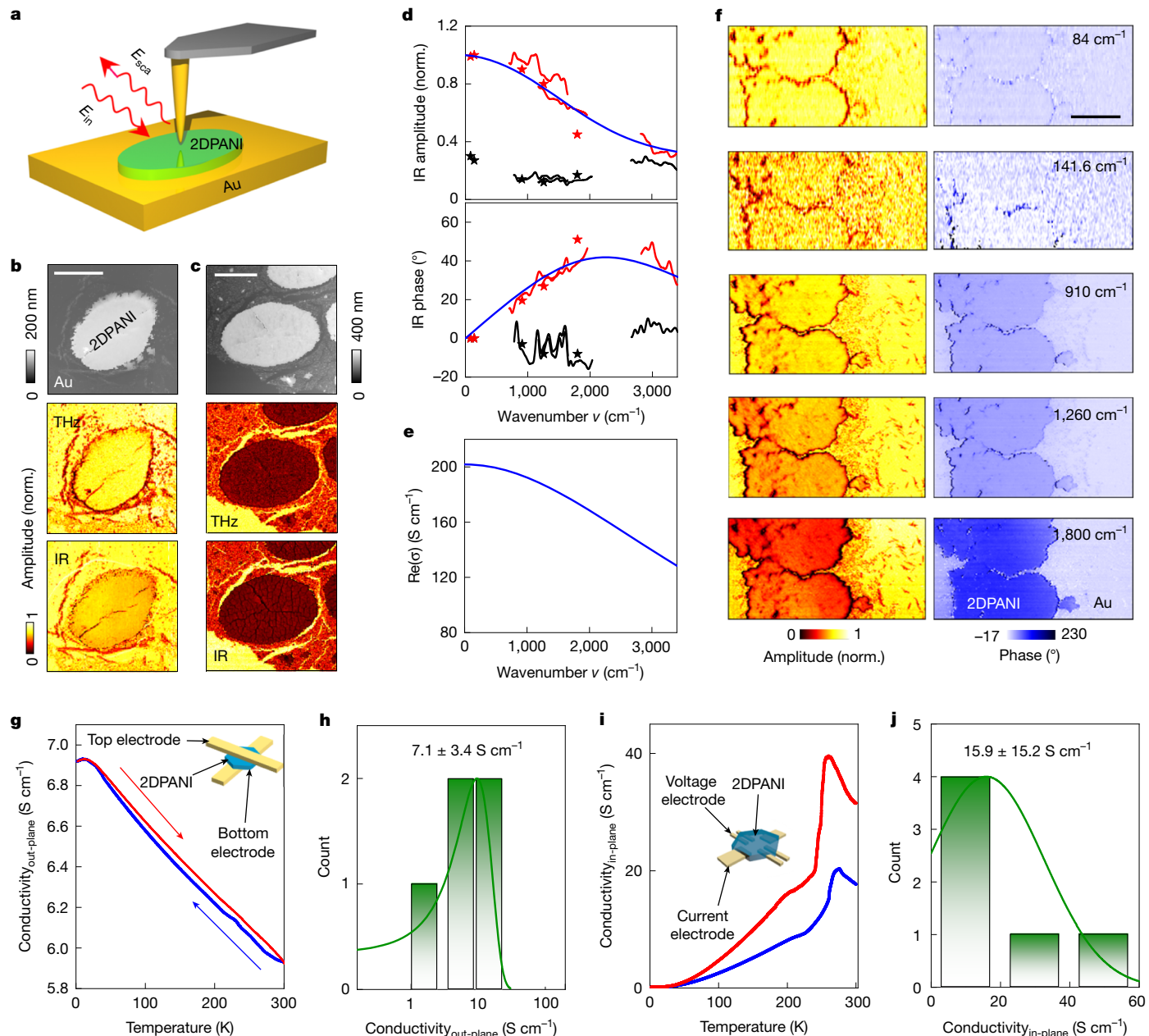


Fig. 4 | THz and IR nanoimaging and nanospectroscopy of 2DPANI. **a**, Illustration of s-SNOM and nano-FTIR spectroscopy. IR or THz radiation of field E_{in} illuminates the tip. The tip-scattered field E_{sca} is recorded while the sample is scanned, yielding nanoscale-resolved IR or THz images. **b,c**, AFM topography (top panel), normalized THz (84 cm^{-1} , middle panel) and IR (910 cm^{-1} , bottom panel) amplitude images of pristine (b) and dedoped (c) 2DPANI flakes on an Au layer. **d**, Normalized (norm.) nano-FTIR amplitude and phase spectra of pristine (red curves and blue fits) and dedoped (black curves) 2DPANI. Each experimental curve corresponds to one bandwidth-limited nano-FTIR spectrum. Red and black stars show normalized THz and IR data obtained from the s-SNOM images

shown in **f** and in Supplementary Fig. 27. **e**, Real part of the conductivity of pristine 2DPANI, obtained from the fit (blue curves) of **d**. **f**, Normalized near-field amplitude and phase images of pristine 2DPANI at different wavenumbers. **g**, Conductivity–temperature curves of vertical micro-device made of an individual 2DPANI flake. **h**, Histograms of out-of-plane electrical conductivity from five vertical micro-devices (see Supplementary Table 3 for details). **i**, Conductivity–temperature curves of lateral micro-device made of an individual 2DPANI flake. **j**, Histograms of in-plane electrical conductivity measured from six lateral micro-devices (see Supplementary Table 4 for details). Scale bars, $10\text{ }\mu\text{m}$ (**b,c**) and $2\text{ }\mu\text{m}$ (**f**).

from 300 to 3 K, which demonstrates a unique metallic charge transport behaviour in the out-of-plane direction of the 2DPANI (Fig. 4g and Supplementary Table 3). An average electrical conductivity of $7.1 \pm 3.4\text{ S cm}^{-1}$ was achieved at room temperature (Fig. 4h). We further used conductive AFM (c-AFM) to evaluate the conductivity of 2DPANI³⁴. The c-AFM analysis reveals an average out-of-plane conductivity of $14.9 \pm 4.6\text{ S cm}^{-1}$ (Supplementary Fig. 32 and Supplementary Table 4). The increased conductivities observed in c-AFM studies are primarily attributed to the reduction of negative effects from structural defects

and the device fabrication process, compared to micro-devices. For the lateral micro-devices, we observed an increase in conductivity with decreasing temperature between 300 and 250 K (Fig. 4i and Supplementary Figs. 33 and 34), indicating metallic-like transport^{35,36}. However, at temperatures below 250 K, a continuous decrease in conductivity was observed. We attribute this behaviour to the presence of abundant structural defects in the 2DPANI flakes, leading to energetic disorder and trap states^{5,37}, which need higher temperatures to overcome. The average electrical conductivity of the in-plane direction is

derived to be 15.9 ± 15.2 S cm $^{-1}$ at room temperature (Fig. 4j and Supplementary Table 5). These findings show that the 2DPANI flakes have anisotropic 3D electrical conductivity with slight superiority along the in-plane direction.

Discussion and conclusion

In summary, we have achieved the synthesis of a multilayer-stacked 2DPANI crystal, which comprises long-range ordered rhombohedral lattices and compact multilayer stacking with Cl $^-$ ion-bridging. This unique structure endows 2DPANI with strong electron delocalization, showing high conductivities in the out-of-plane direction (roughly 15 S cm $^{-1}$). More importantly, the out-of-plane transport follows a metal-like behaviour with a superior conductivity that has not been observed in other conducting polymer materials (Supplementary Table 6) 25,34,38 . Our findings provide important experimental insights into realizing the metallic state of conducting polymers in extended dimensions (for example, out-of-plane direction) through enhancing the intermolecular ordering and electronic coupling between polymer chains and layers. This discovery will open up new possibilities for the development of 3D organic metals for both fundamental physics studies and device applications.

Online content

Any methods, additional references, Nature Portfolio reporting summaries, source data, extended data, supplementary information, acknowledgements, peer review information; details of author contributions and competing interests; and statements of data and code availability are available at <https://doi.org/10.1038/s41586-024-08387-9>.

1. Chiang, C. K. et al. Electrical-conductivity in doped polyacetylene. *Phys. Rev. Lett.* **39**, 1098–1101 (1977).
2. Phillips, P. & Wu, H. L. Localization and its absence—a new metallic state for conducting polymers. *Science* **252**, 1805–1812 (1991).
3. Kohlman, R. S. et al. Limits for metallic conductivity in conducting polymers. *Phys. Rev. Lett.* **78**, 3915–3918 (1997).
4. Kang, K. et al. 2D coherent charge transport in highly ordered conducting polymers doped by solid state diffusion. *Nat. Mater.* **15**, 896–902 (2016).
5. Noriega, R. et al. A general relationship between disorder, aggregation and charge transport in conjugated polymers. *Nat. Mater.* **12**, 1038–1044 (2013).
6. Wang, Z. H., Li, C., Scherr, E. M., Macdiarmid, A. G. & Epstein, A. J. Three dimensionality of metallic states in conducting polymers: polyaniline. *Phys. Rev. Lett.* **66**, 1745–1748 (1991).
7. Jeon, D., Kim, J., Gallagher, M. C. & Willis, R. F. Scanning tunneling spectroscopic evidence for granular metallic conductivity in conducting polymeric polyaniline. *Science* **256**, 1662–1664 (1992).
8. Xie, J. et al. Intrinsic glassy-metallic transport in an amorphous coordination polymer. *Nature* **611**, 479–484 (2022).
9. Bubnova, O. et al. Semi-metallic polymers. *Nat. Mater.* **13**, 190–194 (2014).
10. Lee, K. et al. Metallic transport in polyaniline. *Nature* **441**, 65–68 (2006).
11. Tang, H. et al. A solution-processed n-type conducting polymer with ultrahigh conductivity. *Nature* **611**, 271–277 (2022).
12. Podzorov, V. Conjugated polymers: long and winding polymeric roads. *Nat. Mater.* **12**, 947–948 (2013).
13. Brondijk, J. J. et al. Two-dimensional charge transport in disordered organic semiconductors. *Phys. Rev. Lett.* **109**, 056601 (2012).
14. Basescu, N. et al. High electrical-conductivity in doped polyacetylene. *Nature* **327**, 403–405 (1987).
15. Sirringhaus, H. et al. Two-dimensional charge transport in self-organized, high-mobility conjugated polymers. *Nature* **401**, 685–688 (1999).
16. Osterbacka, R., An, C. P., Jiang, X. M. & Vardeny, Z. V. Two-dimensional electronic excitations in self-assembled conjugated polymer nanocrystals. *Science* **287**, 839–842 (2000).
17. Jin, E. Q. et al. Two-dimensional sp $(^2)$ carbon-conjugated covalent organic frameworks. *Science* **357**, 673–676 (2017).
18. Liu, W. et al. A two-dimensional conjugated aromatic polymer via C-C coupling reaction. *Nat. Chem.* **9**, 563–570 (2017).
19. Gutzler, R. & Perepichka, D. F. π -Electron conjugation in two dimensions. *J. Am. Chem. Soc.* **135**, 16585–16594 (2013).
20. Jing, Y. & Heine, T. Making 2D topological polymers a reality. *Nat. Mater.* **19**, 823–824 (2020).
21. Springer, M. A., Liu, T. J., Kuc, A. & Heine, T. Topological two-dimensional polymers. *Chem. Soc. Rev.* **49**, 2007–2019 (2020).
22. Galeotti, G. et al. Synthesis of mesoscale ordered two-dimensional π -conjugated polymers with semiconducting properties. *Nat. Mater.* **19**, 874–880 (2020).
23. Wang, M. et al. Exceptionally high charge mobility in phthalocyanine-based poly(benzimidazobenzophenanthroline)-ladder-type two-dimensional conjugated polymers. *Nat. Mater.* **22**, 880–887 (2023).
24. Liu, K. J. et al. On-water surface synthesis of crystalline, few-layer two-dimensional polymers assisted by surfactant monolayers. *Nat. Chem.* **11**, 994–1000 (2019).
25. Zhang, T. et al. Engineering crystalline quasi-two-dimensional polyaniline thin film with enhanced electrical and chemiresistive sensing performances. *Nat. Commun.* **10**, 4225 (2019).
26. Tan, K. T. et al. Covalent organic frameworks. *Nat. Rev. Methods Primers* **3**, 1 (2023).
27. Qi, H. Y. et al. Near-atomic-scale observation of grain boundaries in a layer-stacked two-dimensional polymer. *Sci. Adv.* **6**, eabb5976 (2020).
28. Galvao, D. S., Dossantos, D. A., Laks, B., Demelo, C. P. & Caldas, M. J. Role of disorder in the conduction mechanism of polyanilines. *Phys. Rev. Lett.* **63**, 786–789 (1989).
29. Kirinichnyi, V. I. Dynamics of spin charge carriers in polyaniline. *Appl. Phys. Rev.* **1**, 021305 (2014).
30. Huber, A. J., Keilmann, F., Wittborn, J., Aizpurua, J. & Hillenbrand, R. Terahertz near-field nanoscopy of mobile carriers in single semiconductor nanodevices. *Nano Lett.* **8**, 3766–3770 (2008).
31. Huth, F. et al. Nano-FTIR absorption spectroscopy of molecular fingerprints at 20 nm spatial resolution. *Nano Lett.* **12**, 3973–3978 (2012).
32. Cvirkovic, A., Ocelic, N. & Hillenbrand, R. Analytical model for quantitative prediction of material contrasts in scattering-type near-field optical microscopy. *Opt. Express* **15**, 8550–8565 (2007).
33. Madsen, G. K. H., Carrete, J. & Verstraete, M. J. BoltzTraP2, a program for interpolating band structures and calculating semi-classical transport coefficients. *Comput. Phys. Commun.* **231**, 140–145 (2018).
34. Liu, S. H. et al. Two-dimensional mesoscale-ordered conducting polymers. *Angew. Chem. Int. Edit.* **55**, 12516–12521 (2016).
35. Kohlman, R. S. et al. Inhomogeneous insulator-metal transition in conducting polymers. *Synthetic Met* **84**, 709–714 (1997).
36. Kohlman, R. S., Joo, J., Min, Y. G., MacDiarmid, A. G. & Epstein, A. J. Crossover in electrical frequency response through an insulator-metal transition. *Phys. Rev. Lett.* **77**, 2766–2769 (1996).
37. Venkateshvaran, D. et al. Approaching disorder-free transport in high-mobility conjugated polymers. *Nature* **515**, 384–388 (2014).
38. Wang, X. et al. High electrical conductivity and carrier mobility in oCVD PEDOT thin films by engineered crystallization and acid treatment. *Sci. Adv.* **4**, eaat5780 (2018).

Publisher's note Springer Nature remains neutral with regard to jurisdictional claims in published maps and institutional affiliations.

Springer Nature or its licensor (e.g. a society or other partner) holds exclusive rights to this article under a publishing agreement with the author(s) or other rightsholder(s); author self-archiving of the accepted manuscript version of this article is solely governed by the terms of such publishing agreement and applicable law.

© The Author(s), under exclusive licence to Springer Nature Limited 2025

Methods

Chemicals and materials

Sodium *n*-octadecyl sulfate, ammonium persulfate, *N,N'*-diphenyl-1,4-phenylenediamine, silver oxide, chloroform, cyclohexane, acetone and hydrochloric acid (37%) were purchased from Sigma-Aldrich. Aniline (more than 99%) was obtained from Alfa Aesar. All the chemicals were used as received. *N,N'*-diphenylcyclohexa-2,5-diene-1,4-diimine was synthesized according to literature.

Synthesis of 2DPANI flakes

The sodium *n*-octadecyl sulfate was dispersed in chloroform (0.13 mg ml⁻¹). Next, 10 µl of the surfactant dispersion was spread on a hydrochloric acid aqueous solution (50 ml, 0.75 M) surface in a glass well with diameter of 60 mm, and it allowed chloroform to evaporate for 20 min. Then, 1 ml of aniline aqueous solution (0.13 M) was added gently to the subphase using a pipette. After standing for 24 h for the diffusion of aniline monomers in the water subphase and interface, 1 ml of ammonium persulfate (0.02 M) was added to the subphase. The glass well was then covered by a glass slide and placed in a refrigerator (Liebherr FKUv 1660 Premium) at 1 °C for reaction. After roughly 3 days, 2DPANI flakes with green colour appeared on the water surface and were fished using arbitrary substrates. It is worth noting that the water solution was still transparent and colourless, indicating that no polymerization occurred in the subphase.

DFT calculations

DFT calculations were carried out using the Vienna ab-initio Simulation Package (VASP) v.5.4.1 (ref. 39). The electronic wave-functions were expanded in a plane-wave basis set with a kinetic energy cut-off of 400 eV. Electron-ion interactions were described using the projector augmented wave method⁴⁰. Generalized gradient approximation (GGA)⁴¹ of the exchange-correlation energy in the form of Perdew-Burke-Ernzerhoff⁴² was applied. The 2DPANI monolayer was modelled by adding a large vacuum space of 10 Å in the direction normal to the monolayer. A Γ-centred grid with 3 × 3 × 1 dimension was used for *k*-point sampling of the Brillouin zone. In the computational protocol for the 3D stacking of 2DPANI the *k*-point grid dimension was changed to 3 × 3 × 3 and Grimme's D2 London dispersion correction⁴³ was applied. For the electronic band structure calculations of 2DPANI, a denser *k*-point grid of 9 × 9 × 1 for the monolayer and 6 × 6 × 6 for the multilayered model was used. For the monolayer of 2DPANI, the unit cell vectors and angles between them were stepwise changed and the position of the atoms in the unit cell was optimized until we obtained a consistent model with the experimental SAED results from TEM.

To obtain the geometry and electronic properties of the fully undoped and HCl doped 2DPANI, several atomistic models were considered. We started with undoped 2DPANI monolayer and then modelled structures with 50 and 100% of -N= groups doped with HCl. The unit cell used in the DFT calculations is composed of diaminobenzoquinonime node and aniline linkers.

Analysis based on the Boltzmann transport equation

The electrical conductivity, σ , was calculated within the constant relaxation-time approximation of the Boltzmann transport equation using the BoltzTraP2 code. The *k* grid of the VASP calculations was interpolated onto a seven-times denser grid. To extract the average effective mass, m , we used the calculated ratio of the electrical conductivity to the scattering time, σ/τ , and furthermore assumed a Drude-like metallic behaviour:

$$\left(\frac{\sigma}{\tau}\right)_{\text{BoltzTraP2}} = \left(\frac{\sigma}{\tau}\right)_{\text{Drude}} = \frac{ne^2}{m}$$

Note that all quantities also depend on the energy E (that is, the chemical potential) at which the conductivity is measured. The second important parameter in this evaluation is the density of charge carriers, n . We assumed that charge carriers within the thermal energy will contribute to the electrical transport:

$$n = \int \text{DOS}(\varepsilon) f' (E - \varepsilon) d\varepsilon,$$

with the derivative of the Fermi function

$$f' (E - \varepsilon) = \frac{\partial f(E - \varepsilon)}{\partial E} = \frac{\partial}{\partial E} (1/(exp[\beta(E - \varepsilon)] + 1)).$$

For the 2DPANI monolayer the effective mass in the *x* and *y* directions, $m_x^* = 81 m_0$ and $m_y^* = 66 m_0$, are slightly different indicating a small in-plane anisotropy. More advanced calculations of the electrical conductivity beyond the constant relaxation-time approximation are beyond the scope of the present paper and will need many more calculations for, for example, the electron–phonon coupling.

ESR

For performing ESR experiments a standard X-band ESR-spectrometer (EMX from Bruker) operating at a microwave frequency of 9.56 GHz and providing magnetic fields up to 9 kOe was used. It is equipped with a He-gas flow cryostat (Oxford Instruments) allowing temperature-dependent measurements between 4 and 300 K. The spin count experiment was done by comparing the ESR intensity of the 2DPANI sample with the standard reference sample Al₂O₃:Cr³⁺ (Ruby) with a known number of spins⁴⁴. The dedoping of 2DPANI was performed in 1 M NH₄OH aqueous solution for 5 min.

Spin count experiment. For this experiment the standard reference sample Al₂O₃ doped by Cr³⁺ (Ruby) with a known number of spins was used. At room temperature, two standard Ruby samples (Ruby 1 and Ruby 2) with a known number of spins were placed into the ESR resonator, Ruby 1 in the centre and Ruby 2 on the inner wall. The ESR signals of both samples measured simultaneously were used to calculate the respective intensities, which are proportional to the number of spins. The intensities are I_{Ruby1} for Ruby 1 sample, and I_{Ruby2} for Ruby 2, respectively, and their ratio is coefficient $C = I_{\text{Ruby1}}/I_{\text{Ruby2}}$. After Step 1, the Ruby 1 sample was replaced with the 2DPANI sample, which was cooled down to the paramagnetic nonconducting regime with almost linear 1/temperature dependence. The Ruby 2 sample, remaining in the resonator, was always at the room temperature of around 300 K. Next, the ESR lines of 2DPANI and Ruby 2 samples were measured simultaneously at different temperatures of 2DPANI sample ranging from 30 to 150 K, yielding the respective intensities I_{PANI} and I_{Ruby2} . The spin number in the sample under study N then can be calculated by comparing the intensities: $N_{\text{2DPANI}} = N_{\text{Ruby1}} \times 2 \times I_{\text{2DPANI}} \times T_{\text{2DPANI}} / (C \times I_{\text{Ruby2}} \times 300)$. Such a calculation was done at every measurement temperature of the 2DPANI sample T_{2DPANI} . As a last step, the average values of the number of spins in 2DPANI sample N_{2DPANI} and the respective error were calculated.

s-SNOM and nano-FTIR spectroscopy

The experimental setups used in this work are based on commercial s-SNOM and nano-FTIR instrumentation from attocube systems AG (formerly from Neaspec GmbH). Each setup comprises an AFM operating in tapping mode, where the tip is oscillating at the cantilever's mechanical resonance frequency Ω .

For IR imaging, the tip was illuminated with the radiation from a frequency-tunable quantum cascade laser (MIRcat, Daylight Solutions). The tip-scattered light was recorded with a pseudo-heterodyne interferometer⁴⁵, simultaneously with topography. To suppress background scattering from the tip shaft and the sample, the mercury cadmium telluride detector signal was demodulated at 3 Ω, yielding

background-free amplitude and phase images s_3 and φ_3 . For Fig. 4b,c, a PtIr-coated AFM tip with an apex radius of 25 nm (NCPt arrow tip, Nanoworld) was used. The tip oscillation amplitude was around 55 nm. For Fig. 4f and Supplementary Fig. 27, Au-coated AFM tips with an apex radius of 30 nm (ATEC-NCAu tip, Nanosensor) were used. The tip oscillation amplitude was around 55 nm.

For THz imaging, the tip was illuminated with the radiation from a wavelength-tunable THz gas laser (SIFIR-50, Coherent Inc.). The tip-scattered light was recorded by synthetic optical holography, simultaneously with topography^{46,47}. THz detection was done with a cryogen-free Ge:Ga photoconductive THz detector (QMC Instruments). The detector signal was demodulated at 3Ω , yielding background-free amplitude and phase images s_3 and φ_3 . For Fig. 4b,c, an Au-coated AFM tip with an apex radius of 500 nm (LRCH, Team Nanotec) was used. The tip oscillation amplitude was around 100 nm. For Fig. 4f and Supplementary Fig. 27, Au-coated AFM tips with an apex radius of 30 nm (ATEC-NCAu tip, Nanosensor) were used. The tip oscillation amplitude was around 55 nm.

All amplitude images were normalized by division to the average s_3 -value of the Au surface. All phase images were referenced by subtraction, such that the φ_3 -value of the Au surface is 0° .

For nano-FTIR spectroscopy, Au-coated AFM tips with an apex radius of 30 nm (ATEC-NCAu tip, Nanosensors) were illuminated by one of the two integrated broadband IR lasers covering the spectral ranges 800–2,000 and 2,700–3,400 cm⁻¹, respectively. Tip oscillation was at 150 kHz and with about 55-nm amplitude. The tip-scattered light was recorded with an integrated asymmetric FTIR spectrometer³¹. By demodulation of the detector signal at 3Ω , we obtained background-free amplitude and phase spectra. The nano-FTIR spectra of the sample (PANI) were normalized to those of the reference sample (Au), yielding $s_3 = s_{\text{PANI},3}/s_{\text{Au},3}$ and $\varphi_3 = \varphi_{\text{PANI},3} - \varphi_{\text{Au},3}$. Both sample and reference spectra are usually obtained by averaging several individual spectra over a period of seconds to minutes to improve the signal-to-noise ratio. In this work, nano-FTIR spectra were obtained in 6.4 min by averaging 15 spectra. The spectral resolution was set to 50 cm⁻¹ and four times zero filling was applied. During the acquisition of these spectra, we identified a drift of the white light position of the interferometer (Supplementary Fig. 35). This leads to a tilt of the phase spectra, which can be mistaken with spectroscopic features of the sample, particularly when broad resonances are studied, such as the one of 2DPANI. Thus, we used a method (Supplementary Fig. 36) to compensate for the white light position drift to obtain the more accurate spectra shown in Fig. 4d.

To avoid contamination of the tip with 2DPANI and subsequent spectroscopy errors, we used for each nano-FTIR measurement a new tip. Slight differences of the tip shape and particularly the tip apex may lead to contrast variations and may explain, for example, the small offset between the two red IR amplitude curves in the top panel of Fig. 4d in the spectral range between 700 and 2,000 cm⁻¹.

Fitting of s-SNOM and nano-FTIR spectroscopic data. To determine the plasma frequency (expressed in this work in wavenumbers) v_p and the d.c. conductivity $\sigma_{\text{d.c.}}$ from the nano-FTIR spectra, we used the finite-dipole model³². The metallized AFM tip was modelled as a prolate spheroid with a major half-axis length $L = 300$ nm and apex radius $R = 30$ nm. For the tip oscillation, we used the experimental value of 55 nm. The empirical model parameter g was set to the typical value $g = 0.7 \times 10^{0.06i}$. The calculated complex-valued scattering coefficient was demodulated at the third harmonic of the tip oscillation frequency.

The pristine 2DPANI is described by an optical conductivity $\sigma(v) = i\varepsilon_0 2\pi c v (1 - \varepsilon(v))$, where ε_0 is the vacuum permittivity, c the light velocity and $\varepsilon(v)$ the dielectric function. Note that $\sigma(v)$ in this general form includes both the optical conductivity of mobile carriers and of excitations from bound charges. We assume that the permittivity can be roughly described by a Drude model, $\varepsilon(v) = \varepsilon_\infty [1 - v_p^2/(v^2 + iv\gamma_p)]$, where v_p is the screened plasma frequency, γ_p the damping factor and

ε_∞ the high-frequency permittivity that includes all non-Drude contributions such as molecular vibrations.

Simultaneous fitting of the nano-FTIR amplitude and phase spectra of pristine 2DPANI yields $\varepsilon_\infty = 5$, $v_p = 3,300$ and $\gamma_p = 4,500$ cm⁻¹. The nano-FTIR amplitude and phase spectra were fitted simultaneously by calculating amplitude and phase spectra with parameter variation in 100 cm⁻¹ steps, respectively, 0.2 steps for ε_∞ and searching the minimum of $\sum_v \text{Abs}(s_{3,\text{exp}}(v)e^{i\varphi_{3,\text{exp}}(v)} - s_{3,\text{calc}}(v)e^{i\varphi_{3,\text{calc}}(v)})^2$.

Vertical 2DPANI micro-device fabrication

We selected 2DPANI flakes under light microscopy to ensure there were no visible defects or cracks on the flakes. A conventional wet transfer technique was used to transfer 2DPANI flakes directly onto the pre-patterned 5-μm-width bottom Au electrodes, which were prepared by e-beam lithography and a lift-off process. To define the vertical electrical 2DPANI channel, a 5-μm-wide strip, orthogonal to the bottom Au electrodes, was patterned above the single 2DPANI flake using electron beam lithography. Following this, a Ti/Au layer was deposited. To avoid penetration, the Ti and Au layers were evaporated without any accelerating voltage, so that they contain very low energy. Besides, the sample holder is cooled with cooling system, which further reduces the likelihood of penetration. After deposition, the lift-off process was used, leaving only the top Au electrodes intact while the remaining areas of the metal layer were removed. The process is illustrated in Supplementary Fig. 30.

Lateral 2DPANI micro-device fabrication

The 2DPANI lateral device with four-point probe configuration was prepared by the wet transfer method on selected flakes. First, the electrodes were fabricated on thermally oxidized silicon wafer (thickness of SiO₂ roughly 300 nm) by conventional e-beam lithography and ion-beam deposition of Ru/Au layers for patterning and metallization, respectively. After lift-off, we directly scooped the 2DPANI flakes that were at the air–water interface of the reaction beaker on the substrates that were prepatterned with a four-probe structure; thus, there was no potential degradation of PANI crystals due to an unexpected chemical reaction. The process is illustrated in Supplementary Fig. 32.

GIWAXS

GIWAXS measurements were carried out at the XRD1 beamline at ELETTRA, Trieste, Italy, at a photon energy of 12.398 keV ($\lambda = 1\text{\AA}$). The detector was a Dectris Pilatus 2 M. The sample-detector distance was 450 mm as calibrated using a silver behenate standard. The incidence angle of the beam was set to 0.12°. The exposure time was 120 s. The resulting images were then analysed with WxDiff⁴⁸. The indexing of the GIWAXS in-plane unit cell was performed by a least-square fitting of the experimental data to the equation $q_{xy} = \sqrt{(ha_{||}^*)^2 + (kb_{||}^*)^2 + (\gamma^*)^2}$ to the experimentally observed in-plane peak positions⁴⁹. The vertical stacking distance d_{001} was directly obtained from the vertical reciprocal lattice vector \mathbf{c}^* . The resulting images were then analysed with WxDiff⁴⁸.

Other characterizations

The morphology and structure of the 2DPANI flakes were investigated by TEM (Zeiss, Libra 200), scanning electron microscopy (Zeiss Gemini 500) and light microscopy (Zeiss) with a Hitachi KP-D50 colour digital CCD camera. High-resolution TEM images were acquired on an image-side spherical-aberration-corrected FEI Titan 80–300 operated at an acceleration voltage of 300 kV. XPS measurements were performed on a PHI-5000C ESCA system with a monochromatic Mg K α X-ray source ($h\nu = 1,253.6$ eV), the Cls value was set at 284.6 eV for charge corrections. Raman spectra and maps were measured on a NT-MDT confocal spectrometer with a 532 nm laser, and the spot size of the laser beam was roughly 0.5 μm. IR spectra were recorded on a FTIR Spectrometer Tensor II (Bruker) with an ATR unit. AFM images were recorded in air on a customized Ntegra Aura/Spectra from NT-MDT with a SMENA head in semicontact mode. The probes have a typical

Article

curvature radius of 6 nm, a resonant frequency of 47–50 kHz and a force constant of 0.35–6.10 N m⁻¹. Height determination and calculation were performed with the software Nova Px v.3.2.5 from NT-MDT and the free software Gwyddion. The structure of 2DPANI was calculated using a tight binding density-functional approach with the DFTB+ package⁵⁰ and 3ob-3-1 parameters dataset^{51,52}. Corresponding SAED patterns of the modelled structure were simulated using CrystalMaker.

Data availability

The data supporting the findings of the study are available in the paper and its Supplementary Information.

39. Kresse, G. & Furthmuller, J. Efficient iterative schemes for ab initio total-energy calculations using a plane-wave basis set. *Phys. Rev. B*, **54**, 11169–11186 (1996).
40. Blochl, P. E. Projector augmented-wave method. *Phys. Rev. B*, **50**, 17953–17979 (1994).
41. Perdew, J. P. et al. Atoms, molecules, solids, and surfaces—applications of the generalized gradient approximation for exchange and correlation. *Phys. Rev. B*, **46**, 6671–6687 (1992).
42. Perdew, J. P., Burke, K. & Ernzerhof, M. Generalized gradient approximation made simple. *Phys. Rev. Lett.*, **77**, 3865–3868 (1996).
43. Grimme, S. Semiempirical GGA-type density functional constructed with a long-range dispersion correction. *J. Comput. Chem.*, **27**, 1787–1799 (2006).
44. Chang, T., Foster, D. & Kahn, A. An intensity standard for electron paramagnetic resonance using chromium-doped corundum ($\text{Al}_2\text{O}_3:\text{Cr}^{3+}$). *J. Res. Natl Bur. Stand.*, **83**, 133–164 (1977).
45. Ocelic, N., Huber, A. & Hillenbrand, R. Pseudoheterodyne detection for background-free near-field spectroscopy. *Appl. Phys. Lett.*, **89**, 101124 (2006).
46. Maissen, C., Chen, S., Nikulina, E., Goyadlinov, A. & Hillenbrand, R. Probes for ultrasensitive THz nanoscopy. *ACS Photonics*, **6**, 1279–1288 (2019).
47. Schnell, M., Carney, P. S. & Hillenbrand, R. Synthetic optical holography for rapid nanoimaging. *Nat. Commun.*, **5**, 3499 (2014).
48. Yuan, Q. et al. Thin film structure of tetraceno[2,3-b]thiophene characterized by grazing incidence X-ray scattering and near-edge X-ray absorption fine structure analysis. *J. Am. Chem. Soc.*, **130**, 3502–3508 (2008).
49. Talnack, F. et al. Thermal behavior and polymorphism of 2,9-didecyldinaphtho[2,3-b:2',3'-f]thieno[3,2-b]thiophene thin films. *Mol. Syst. Des. Eng.*, **7**, 507–519 (2022).
50. Aradi, B., Hourahine, B. & Frauenheim, T. DFTB+, a sparse matrix-based implementation of the DFTB method. *J. Phys. Chem. A*, **111**, 5678–5684 (2007).
51. Gaus, M., Goez, A. & Elstner, M. Parametrization and benchmark of DFTB3 for organic molecules. *J. Chem. Theory Comput.*, **9**, 338–354 (2013).
52. Lu, X. Y., Gaus, M., Elstner, M. & Cui, Q. Parametrization of DFTB3/3OB for magnesium and zinc for chemical and biological applications. *J. Phys. Chem. B*, **119**, 1062–1082 (2015).

Acknowledgements R.D., R.H. and X.F. acknowledge the funding support from EU Graphene Flagship (GrapheneCore3, grant no. 881603), ERC starting grant (FC2DMOF, grant no. 852909), ERC Consolidator grant (no. T2DCP). R.D., X.F., T.B. and T.H. thank Deutsche Forschungsgemeinschaft within CRC 1415 (Chemistry of Synthetic Two-Dimensional Materials, grant no. 417590517), as well as the Center of Advancing Electronics Dresden (caed). T.Z. acknowledges the funds from the National Natural Science Foundation of China (grant no. 52322316) and the Excellent Youth Foundation of Zhejiang Province of China (grant no. RG25EO30003). R.D. acknowledges the National Natural Science Foundation of China (grant nos. 22272092 and 22472085). S.C. acknowledges the funds from the National Natural Science Foundation of China (grant nos. 61988102, 6242200987 and 62301319) and the Science and Technology Commission of Shanghai Municipality (grant nos. 23010503400 and 23ZR1443500). We acknowledge P. Mack and L. Kaeselitz from Thermo Fisher Scientific (UK) for the assistance of μ XPS characterization. R.H. acknowledges financial support from Grant CEX2020-001038-M funded by the Spanish MICIU/AEI/1013039/501100011033 and Grants RTI2018-094830-B-I00 and PID2021-123949OB-I00 funded by the Spanish MICIU/AEI/1013039/501100011033 and by ERDF/EU. P.L. acknowledges the National Natural Science Foundation of China (grant no. 62075070), the Hubei Optical Fundamental Research Center, and the Innovation Fund of WNLLO. T.B., T.H. and P.P.P. thank ZIH Dresden for providing computational resources. We acknowledge ELETTRA Sincrotrone Trieste for providing access to its synchrotron radiation facilities and we thank L. Barba for assistance in using beamline XRD1. The research leading to this result has been supported by the project CALIPSOplus under grant agreement no. 730872 from the EU Framework Programme for Research and Innovation HORIZON 2020.

Author contributions T.Z., R.D., R.H. and X.F. conceived the idea and supervised the project. T.Z. and P.Z. performed the synthesis and basic characterization and data analysis. S.X. supported the experiment of model reaction. S.C., P.L., L.M. and R.H. carried out the terahertz and IR nanospectroscopy measurements and analysis. P.P.P., T.B. and T.H. implemented the DFT calculations. H.Q., U.K., Z.L. and E.Z. performed SAED and HRTEM characterization and analysis. N.N.N. carried out c-AFM and analysis. N.N.N., J.Y., W.Z. and S.S.P.P. carried out the study of micro-devices. A.A., V.K., and B.B. performed ESR study. M.H. and S.C.B.M. supported GIWAXS study. All authors discussed the results and assisted with manuscript composition.

Competing interests R.H. is a cofounder of Neaspec GmbH, which is now a part of attocube systems AG, a company producing scattering-type scanning near-field optical microscope systems, such as the ones used in this study. The remaining authors declare no competing interests.

Additional information

Supplementary information The online version contains supplementary material available at <https://doi.org/10.1038/s41586-024-08387-9>.

Correspondence and requests for materials should be addressed to Thomas Heine, Renhao Dong, Rainer Hillenbrand or Xinliang Feng.

Peer review information *Nature* thanks Reverent Crispin, Wenping Hu and the other, anonymous, reviewer(s) for their contribution to the peer review of this work.

Reprints and permissions information is available at <http://www.nature.com/reprints>.